Photopyroelectric thermal wave detection via contactless capacitive polyvinylidene fluoride (PVDF)-metal probe-tip coupling

Marek Mieszkowski, Kwan F. Leung, and Andreas Mandelis

Photoacoustic and Photothermal Sciences Laboratory, Department of Mechanical Engineering, and Ontario Laser and Lightwave Research Center, University of Toronto, Toronto, Ontario M5S1A4, Canada

(Received 16 June 1988; accepted for publication 8 September 1988)

In the past, thin-film photopyroelectric detectors have provided a simple means of measuring thermal properties of solid samples. This article presents a theoretical model and experimental results demonstrating a new contactless capacitively coupled photopyroelectric detection technique. The photopyroelectric (P^2E) effect with contactless capacitance PVDF-metal probe-tip coupling was demonstrated and used to obtain thermal information from a solid. Due to the small diameter of the probe, the local values of the thermal wave field in the solid were measured. The modulated photothermal source on the surface of the sample induces an oscillating temperature field in the pyroelectric material, which produces a displacement current proportional to the temperature change. The metalized surface of the pyroelectric thin film and a metal tip electrode facing the opposite unmetalized surface form a capacitor which is charged at the same frequency as the modulated light beam. The oscillating capacitive voltage provides a noncontact mechanism to extract photothermal information, since the electric field generated in the capacitor does not require plate contact with the PVDF element.

INTRODUCTION

Recently, many useful applications of the photopyroelectric (P^2E) effect have been reported regarding the measurement of both thermal and optical absorption properties of solids.[1,2] The photopyroelectric effect has provided a calorimetric method in which a thin-film pyroelectric detector produces a voltage proportional to its surface temperature change due to the propagation of thermal waves through a sample in intimate contact with the pyroelectric thin-film, polyvinylidene fluoride (PVDF). This technique is capable of providing thermal information about the bulk of the samples under investigation, when used in a scanning mode.[3] The signal detection mechanism involves the generation of an ac potential across the pyroelectric thin film due to charge displacement in the polymer matrix induced by film temperature changes. Potential differences between opposite film surfaces can be measured using thin metal electrodes of several hundred Å thickness deposited on both sides of PVDF.

In this work, we report a new method of photothermal wave signal detection from PVDF films using single surface electroded detectors and a remote (i.e., noncontacting) metal pin positioned close to the unmetalized surface. The charge differences generated by the P^2E effect between the PVDF surface and the narrow metallic pin flat tip create an electrical element geometry equivalent to a parallel-plate capacitor with unequal plate areas. With the new capacitively coupled P^2E technique, the local thermal wave signal can be detected and the thermal wave field imaged by recording the signal at different scanning positions.

I. INSTRUMENTATION

A. P^2E signal generation and apparatus

The use of a laser to thermally excite a material allows the generation of a spatially well-defined thermal wave source in a sample. The acquisition of thermal wave information in P^2E detection is achieved via a single frequency harmonic excitation and lock-in detection of pyroelectric signals using a sinusoidally modulated cw optical source irradiating the sample. The new capacitively coupled photopyroelectric technique reported in this work is similar to the conventional photopyroelectric technique but for the additional capacitance in the space formed between the PVDF thin film and the metal probe pin tip. The metal pin does not have to be in contact with the PVDF thin film since the interplate electric field can propagate through air or vacuum. In the present work, we demonstrate the feasibility of detection of a pyroelectric voltage generated by this process. This is implemented by using a PVDF film with a metal electrode on one side and a second electrode in the form of a metal pin scanning the opposite surface of PVDF at a working distance of 0.1 mm. The thermal wave field in the PVDF film can be expressed as[4]

$$T(x,y,z,t) = T_{ac}(x,y,z)\exp\{j[\omega t + \psi(x,y,z)]\} + T_{dc}(x,y,z) + T_0, \tag{1}$$

where T_0 is the ambient temperature; $T_{ac}(x,y,z)$ is the amplitude of the ac component of the temperature field in the pyroelectric film; $\psi(x,y,z)$ is the phase of the ac component of the temperature field; and $T_{dc}(x,y,z)$ is the magnitude of the dc component of the temperature field in the pyroelectric film for a given configuration and angular frequency ω. Under photothermal excitation, the pyroelectric voltage is given by[5]

$$U(x,y,t) = \frac{pL_{\rm PVDF}}{\epsilon}\langle T(x,y,z,t)\rangle_z. \tag{2}$$

In Eq. (2), p is the PVDF pyroelectric coefficient (30×10^{-6} C/m^{2}K),[5] $L_{\rm PVDF}$ is the film thickness, ϵ is the film dielectric constant (12 for Kynar PVDF),[5] and

$\langle T(x,y,z,t)\rangle_z$ is the spatially averaged temperature field in the pyroelectric film defined as[6]

$$\langle T(x,y,z,t)\rangle_z = \frac{1}{L_{\mathrm{PVDF}}}\int_0^{L_{\mathrm{PVDF}}} T(x,y,z,t)dz. \quad (3)$$

Equation (2) is strictly valid only for 1-D temperature distribution when $T(x,y,z)$ is not a function of x, y coordinates or in the case when the detection electrodes are infinitesimally small. In general, PVDF film with metal electrodes on both sides forms a capacitor, which acts like an integrating detector, and we can express the voltage developed between its plates as

$$\langle U\rangle_{x,y} = \frac{1}{a^2}\int_{-a/2}^{a/2}\int_{-a/2}^{a/2} U(x+x',y+y')dx'\,dy', \quad (4)$$

where a is the length of a square tip of a detector pin or the length of the square electrode on both sides of PVDF film. From Eqs. (2)–(4) we have

$$U_{\mathrm{ac}}(x,y,\omega t) = \frac{p}{\epsilon a^2}\int_{-a/2}^{a/2}\int_{-a/2}^{a/2}\int_0^{L_{\mathrm{PVDF}}} T_{\mathrm{ac}}(x+x',y+y',z) \times \sin[\omega t+\psi(x+x',y+y',z)]dz\,dx'\,dy', \quad (5)$$

where U_{ac} is the ac voltage observed between the plates of the capacitor at position (x,y) on the film, and that point corresponds to the midpoint between the electrode edges. The electric displacement current through the PVDF film is then given by

$$I_D(t) = A\frac{d\langle P(t)\rangle_z}{dt}, \quad (6)$$

where A is the surface area of the electrode, and

$$\langle P(t)\rangle_z \equiv \frac{1}{L_{\mathrm{PVDF}}}\int_0^{L_{\mathrm{PVDF}}} P(z,t)dz \quad (7)$$

is the spatially averaged dipole moment per unit volume. The oscillating dipole moment responsible for I_D sets up an electric field which penetrates the space between the PVDF film and the probe metal tip. Therefore, the metal tip can pick up an electrical signal without touching the PVDF film, thus generating a purely contactless detection technique for the photopyroelectric effect.

The schematic diagram of the experimental system used for the detection of photothermal waves via the capacitively coupled pyroelectric technique is shown in Fig. 1. In this particular arrangement, the tip diameter was 0.8 mm, the laser beam waist was 0.1 mm, and the PVDF thickness was 28 μm. A copper sample was placed on top of the (electroded) surface of the PVDF film using conductive adhesive so as to form an opaque surface layer in agreement with the configuration of Fig. 1. The copper sample was 0.127 mm thick. A 10-mW, He–Ne laser beam from a Hughes Aircraft Company laser (model 3235H-PC) was amplitude modulated in the frequency range from 0.5 to 100 Hz using an ISOMET acousto-optic (A/O) modulator (model 1201E-2) or an AMKO mechanical chopper (model OC 4000). The A/O driver was a Hewlett–Packard waveform generator (model 3312A). The schematic diagram of the detection system is shown in Fig. 2. Considerable effort has been made to eliminate acoustic noise pickup due to the piezoelectric effect in the PVDF film. The acoustical noise due to the vibration of the mechanical chopper was damped by inserting foam underneath that device. The detector was properly shielded in order to reduce any electromagnetic noise from leaking into the detection system, by using a PVDF housing design modified in comparison to the one used in earlier studies.[7] Furthermore, the electromagnetic noise was reduced by eliminating all the ground loops via proper grounding. Figure 2 indicates that the active element of the detector (G) was actually a brass metal pin underneath the nonelectroded PVDF thin film (E). The entire detector assembly was surrounded by a metallic shielding wall (F). The possibility of piezoelectric signal generation by PVDF, which also acts as a piezoelectric transducer,[8] was also investigated. Operationally, the clamping of the PVDF transducer was arranged so that piezoelectric microphonics almost entirely disappeared from the screen of the signal monitoring oscilloscope. Under these conditions, direct laser heating of the PVDF

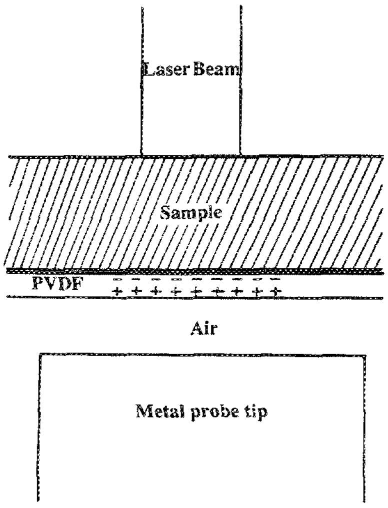

FIG. 1. Schematic diagram of the capacitively coupled pyroelectric geometry used for detection of thermal waves in condensed phase materials.

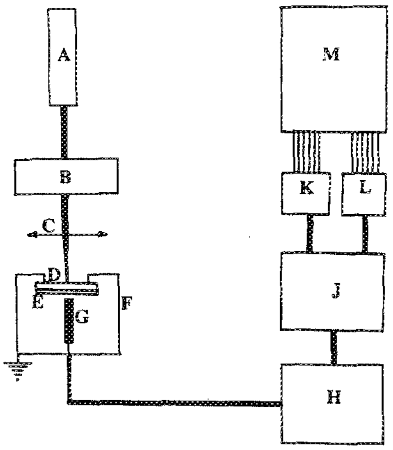

FIG. 2. Schematic diagram of detection electronics. A: He–Ne laser, B: acousto–optic modulator or mechanical chopper, C: lens, D: copper strip, E: PVDF film, F: metal shield, G: metal tip, H: preamplifier, J: lock-in analyzer, L: in-phase of signal to channel 0 of A/D converter, K: quadrature of signal to channel 1 of A/D converter, M: PDP/11 microcomputer.

film produced pyroelectric signal levels at least two orders of magnitude higher than background microphonics. Furthermore, Tam and Coufal have reported[8] that extremely high attenuation of parasitic piezoelectric effects occurs in PVDF, and very good acoustic coupling (e.g., a thin-film water interface) is required between the transducer (PVDF) and the mechanically excited sample. The experiments reported in this work only required simple contact between sample and PVDF, and the resulting signals were consistent with heat conduction from sample to backing. Similar observations ruling out piezoelectric contributions to PVDF-generated signals, with the transducer operating in the pyroelectric mode, have been reported previously.[9]

B. Equivalent electronic circuit layout

The electronic equivalent circuit diagram for the contactless detection of the photopyroelectric system described in Fig. 2 is shown in Fig. 3. For all practical applications and in the modulation frequency range between 0.5 to 100 Hz, the internal film resistance $R_{\rm PVDF}$ can be neglected. The reason is that the impedance of the $R_{\rm PVDF}$ is very large compared to the impedance of the capacitor $C_{\rm PVDF}$. $C_{\rm PVDF}$ is the capacitance of the PVDF thin film and C_c is the capacitance between the nonelectroded surface of the PVDF film and the brass metal pin. R_{Ipa} is the resistance in the preamplifier. C_I is the combined capacitance of the preamplifier, C_{Ipa} and the capacitance of the cable, C_{Ic}:

$$C_I = C_{Ipa} + C_{Ic}.$$

The operational amplifier symbol A represents the circuit of the amplification stage of the ITHACO 1201 amplifier used in this work.

II. FREQUENCY-DOMAIN PHOTOPYROELECTRIC (P^2E) CIRCUIT ANALYSIS AND ELECTRICAL PARAMETER MEASUREMENT

The experimental technique developed in this work involves the steady-state response of the electrical network shown in Fig. 3 to a harmonic optical intensity modulation at frequency $f = \omega/2\pi$. The input excitation due to the modulated laser beam can be written as

$$U(\omega,t) = U_0(\omega)\, e^{j\omega t}, \tag{8}$$

where $U_0(\omega)$ is the frequency dependent voltage amplitude registered across the PVDF detector. Then the synchronous input voltage across the amplifier A can be written as follows:

$$U_{in}(\omega,t) = A(\omega)\, U_0(\omega)\, e^{j\omega t}. \tag{9}$$

In Eq. (9)

$$A(\omega) \equiv \frac{U_{in}(\omega)}{U(\omega)} = A_0(\omega)\, e^{j\phi(\omega)} \tag{10}$$

is the voltage transfer function (voltage reduction factor) due to the electrical network shown in Fig. 3. $U_{in}(\omega,t)$ is the input voltage seen by the amplifier A of Fig. 3. The voltage transfer function $A(\omega)$ of an ideal amplifier A has been calculated analytically in the Appendix. Its amplitude $A_0(\omega)$

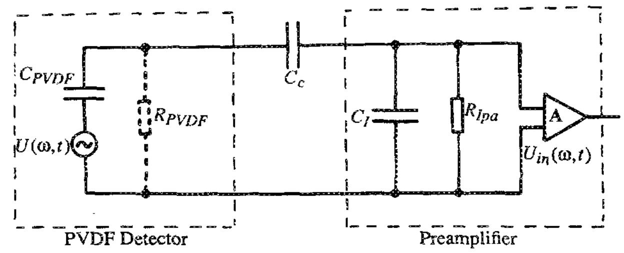

FIG. 3. Electrical equivalent circuit diagram for contactless photopyroelectric detection. Symbols are explained in the text. $U(\omega,t)$ is the P^2E voltage generated across the PVDF film. $U_{in}(\omega,t)$ is the input voltage across the amplifier A.

and phase $\phi(\omega)$ are given by Eqs. (A14) and (A15), respectively:

$$A_0(\omega) = \frac{\omega C_{\rm EFF} R_I}{\{1 + [\omega R_I (C_{\rm EFF} + C_I)]^2\}^{1/2}}, \tag{11}$$

and

$$\phi(\omega) = \tan^{-1}\left(\frac{1}{\omega R_I (C_{\rm EFF} + C_I)}\right), \tag{12}$$

where

$$C_{\rm EFF} \equiv \frac{C_c C_{\rm PVDF}}{C_c + C_{\rm PVDF}} \tag{13}$$

is the effective capacitance resulting from the combination of the PVDF equivalent capacitance $C_{\rm PVDF}$ and the coupling capacitance C_c. $C_{\rm EFF}$ can be measured experimentally. Equation (13) shows that the effective capacitance is a function of the PVDF film thickness, the geometry of the electroded upper surface of the PVDF detector, the geometry of the metal tip, and the distance R between the metal tip and the PVDF film. The values of the capacitances C_c and $C_{\rm PVDF}$ can be accurately estimated for very small separations R. Using the parallel-plate capacitor formula, the value of the capacitance can be estimated as follows:

$$\lim_{R \ll S^{1/2}} C_{\rm EFF}(R) \rightarrow C(R) = \epsilon\epsilon_0 (S/R), \tag{14}$$

where S is the surface area of the flat top of the metal tip. For large values of R, however, one must use more complete three-dimensional models.[10] An "ideal" electrical network and amplifier (A) (Fig. 3) would exhibit infinite input resistance R_I and zero input capacitance C_I

$$R_I = \infty, \quad C_I = 0. \tag{15}$$

Substituting Eq. (15) into Eqs. (11) and (12), we obtain the "ideal" behavior of the detection circuitry

$$A(\omega) \approx 1, \quad \phi(\omega) \approx 0. \tag{16}$$

This indicates that an ideal amplifying circuit in the configuration of Fig. 3 preserves signal amplitude undistorted and phase unaltered, as expected.

In order to quantitatively characterize the behavior of the equivalent electrical network of the photopyroelectric system shown in Fig. 3, the pertinent electrical parameters were measured using standard electrical measurement methods as follows:

$$R_{Ipa} \approx 400\ \mathrm{G\Omega} \pm 20\%,$$
$$C_{Ipa} \approx 16\ \mathrm{pF} \pm 20\%.$$

In order to determine R_{Ipa}, a dc voltage was applied to the input of the preamplifier A directly first and then through a 1-GΩ resistor (R_A). The input resistance of the nonideal amplifier can then be determined from the following equation (see Fig. 3):

$$R_{Ipa} = \left(\frac{U_{\text{out 2}}}{U_{\text{out 1}} - U_{\text{out 2}}}\right) R_A, \qquad (17)$$

where R_A is the resistor in series with R_I; $U_{\text{out 1}}$ is the dc voltage across the output of the preamplifier without resistor R_A; and $U_{\text{out 2}}$ is the dc voltage across the output of the preamplifier with resistor R_A in series with R_I. Measurements using the quantities in Eq. (17) yielded the value of R_{Ipa} (400 G$\Omega \pm 20\%$). In order to determine C_I, an ac voltage was applied to the input of the preamplifier directly and via a 200-MΩ resistor (R_A). The input capacitance of the preamplifier C_{Ipa} was then determined from the equation

$$C_{Ipa} = \left[\left(\frac{U_{\text{out 1}}}{U_{\text{out 2}}}\right)^2 - 1\right]^{1/2} \Big/ \omega R_A . \qquad (18)$$

The capacitance C_I of the connecting cable (coax type RG58; 3 ft) together with that of the metal shielding box (see Fig. 2) was measured, and its value was found to be

$$C_I = (104 \pm 1)\mathrm{pF}.$$

The resistance between the shielding grid and central wire of the coaxial cable was found to be negligible in comparison with the measured R_{Ipa} of the preamplifier. The total capacitance C_I of the network (see Fig. 3) was thus found to be

$$C_I = C_{Ic} + C_{Ipa} = 104\ \mathrm{pF} + 16\ \mathrm{pF} = 120\ \mathrm{pF}. \qquad (19)$$

The total resistance R_I of the network is approximately equal to that of the preamplifier given by Eq. (17)

$$R_I \approx R_{Ipa} = 400\ \mathrm{G\Omega}. \qquad (20)$$

In order to estimate the value of the capacitance C_{PVDF}, the parallel-plate capacitor formula Eq. (14) was used:

$$C_{\text{PVDF}} = \epsilon\epsilon_0 \frac{S}{L_{\text{PVDF}}} \approx 1.9\ \mathrm{pF}, \qquad (21)$$

where $S = \pi r^2$ is the effective surface area of both plates which is equal to 0.503 mm^2. The radius r of the exposed PVDF film electrodes in our experiment was 0.4 mm (equal to the radius of the metal probe). L_{PVDF} stands for the distance between plates (equal to PVDF film thickness of 28 μm). Similarly, in order to estimate the value of the coupling capacitor C_c in Fig. 3, the parallel-plate capacitor formula with separation $R = 0.1$ mm gave

$$C_c \approx 0.044\ \mathrm{pF}. \qquad (22)$$

An estimated value of C_{EFF} was thus obtained using Eq. (13):

$$C_{\text{EFF}} \approx 0.043\ \mathrm{pF}. \qquad (23)$$

In the case of zero separation between pyroelectric film and probe tip, Eqs. (13) and (21) yield

$$\lim_{R\to 0} C_{\text{EFF}} = \lim_{R\to 0}\left(\frac{C_c C_{\text{PVDF}}}{C_c + C_{\text{PVDF}}}\right) = C_{\text{PVDF}} \approx 1.9\ \mathrm{pF}. \qquad (24)$$

As can be seen from Eqs. (23) and (24), the effective capacitance C_{EFF} is very small compared with the input capacitance C_I given by Eq. (19). From experiments with the simulated electrical network shown in Fig. 3, the value of C_{EFF} measured indirectly at contact was found to be

$$C_{\text{EFF}} = 0.6\ \mathrm{pF}. \qquad (25)$$

The discrepancy between the theoretical value, Eq. (24), which is a lower bound on C_{PVDF} according to the generalized 3-D capacitance model presented by Mandelis[10] and the experimental value, Eq. (25), can be accounted for by hypothesizing that there was no perfect contact between flat pin and PVDF film, due to roughness on both surfaces. Imperfect contact leading to an effective separation of 0.005 mm would result in a coupling capacitance $C_c \approx 0.88$ pF predicted by Eq. (14), leading to the C_{EFF} value given by Eq. (25).

In Fig. 4, the voltage response of the theoretical circuit equivalent to the photopyroelectric experimental system is shown. Using Eqs. (11)–(13), (21), and (22) the ampli-

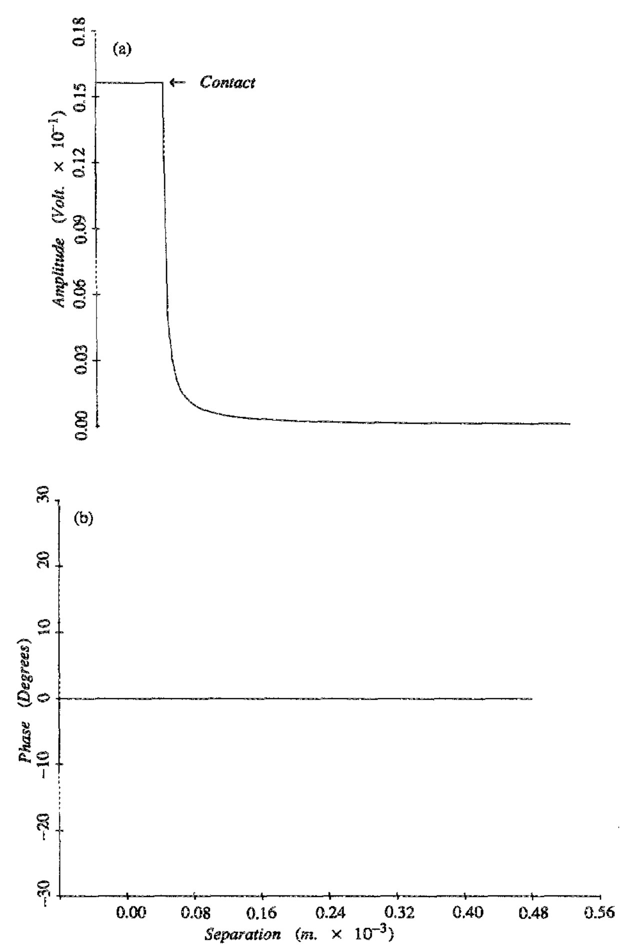

FIG. 4. (a) Theoretical voltage amplitude response, Eq. (11) with $R_I = 400$ GΩ, $C_I = 120$ pF, and $r_0 = 0.4$ mm, where C_{EFF} and C_c are capacitances calculated from Eqs. (13) and (14), respectively. The plateau of the curve corresponds to the theoretical value for perfect contact with no air gap between the tip and PVDF film. (b) Theoretical phase response, Eq. (12), with the same electrical parameters as in part (a).

tude and phase response are calculated as functions of separation R at a constant frequency. It should be pointed out that the value calculated with Eq. (22) is appropriate only for very small plate separation.[10] In the experimental configuration, the capacitance C_{EFF} decreases with separation R at a slower rate than the capacitance calculated from Eq. (14) due to 3-D effects. Another important aspect of contactless detection is that when the metal tip is removed further from the PVDF film surface, the film surface area contributing to the P^2E signal becomes larger due to the spatial divergence of the electric field lines between the effective capacitor plates. Furthermore, the photothermal wave temperature field inside the PVDF thin film is three dimensional in nature,[11] and so is the charge distribution inside the PVDF thin film.

A harmonically modulated laser light causes a voltage $U(\omega,t)$ to appear across the PVDF film, as shown in Fig. 3 due to the photopyroelectric effect. When the separation R is fixed, the value of the capacitance C_c (and thus C_{EFF}) is also fixed in the equivalent circuit of Fig. 3. Figure 5 shows the theoretical voltage transfer function amplitude $A_0(\omega)$ and phase lag $\phi(\omega)$, when the metal pin surface is touching the PVDF thin film. It can be seen that the equivalent electrical network relevant to this work does not introduce any distortion in the frequency range between 0.5 and 100 Hz. However, the equivalent electrical network predicts that the amplitude will be distorted at frequencies well below 0.1 Hz while the phase will be distorted at frequencies below 0.5 Hz. The results of Fig. 5 indicate that the network transfer function contributes a flat response in the frequency range of interest and thus may be neglected in the analysis of capacitively detected P^2E signals.

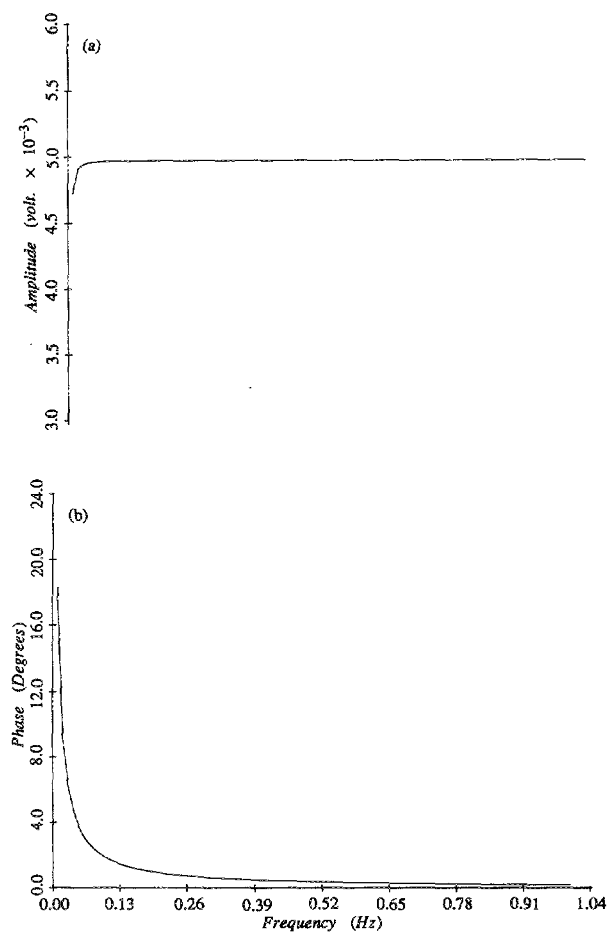

FIG. 5. (a) Theoretical voltage amplitude frequency response with $R_f = 400$ GΩ, $C_f = 120$ pF, and $C_{EFF} = 0.6$ pF; (b) theoretical voltage phase frequency response with the same parameters.

III. EXPERIMENTAL BEHAVIOR OF P^2E NETWORK

A. Signal dependence on separation distance (R)

In order to understand the response of our experimental P^2E network, an electrical simulation circuit was assembled using the sinusoidal voltage from the function generator applied to the upper metal electrode of PVDF film as shown in Fig. 6. The simulation set up was exactly the same as that of Fig. 2, except for the signal from the function generator replacing the pyroelectric ac voltage output of the photothermally excited PVDF detector in the actual experiments. In this fashion, the constant output amplitude and phase of the sine wave generator were established as functions of frequency, effectively rendering $U_0(\omega)$ in Eq. (8) constant. This assumption is consistent with the derivation of Eqs. (11) and (12) (see Appendix) and is required in order to carry out meaningful comparisons between the theory developed in Sec. II above and the experimental network response. It is well known[6,12] that the PVDF detector introduces its own strong photothermal response as a function of modulation frequency. The output voltage amplitude of the experimental simulation is shown in Fig. 7(a) and the phase response is shown in Fig. 7(b), both as functions of the interplate separation (R). The observed behavior of the electrical network is similar to the expected theoretical behavior, however, the output voltage in the experimental simulation decreases more slowly than the theoretically predicted result, Fig. 4(a). It should be recalled that the theoretical circuit results are based on the assumption that the C_{PVDF} and C_c are given by the parallel-plate capacitor approximation. The fact that the R dependence of C_{EFF} is more complicated than that described by Eqs. (13) and (14) primarily due to three-

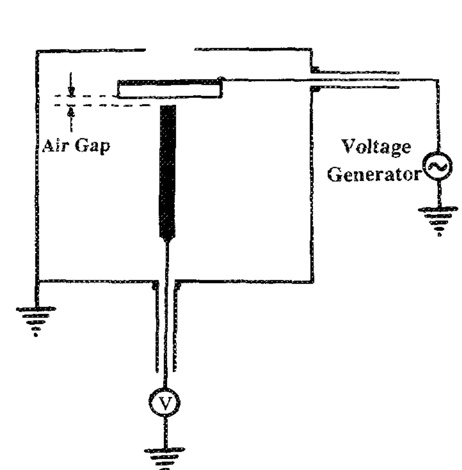

FIG. 6. Electrical stimulation of ac network set up to test the amplitude response of the detection circuit of Fig. 3.

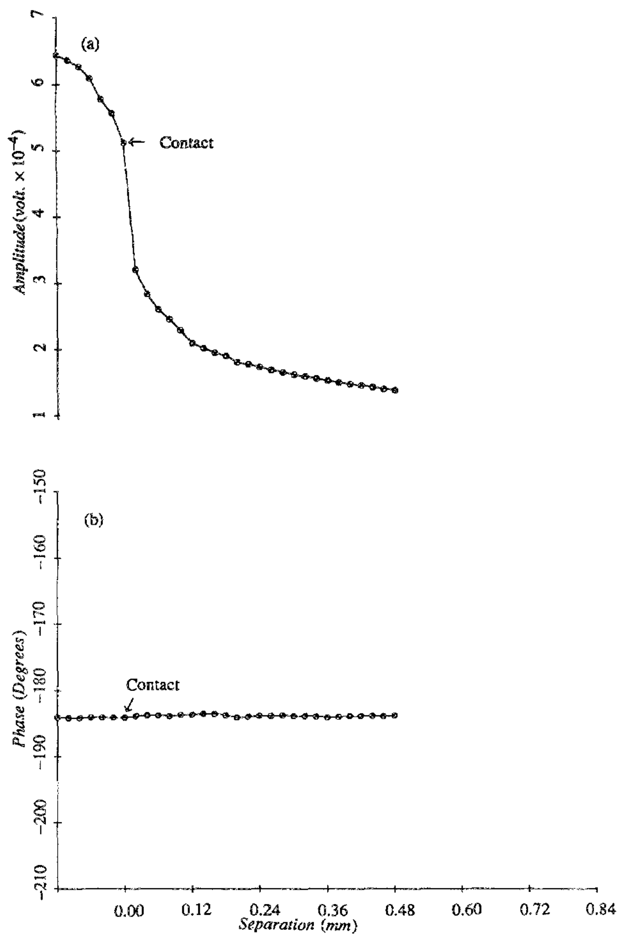

FIG. 7. (a) Experimental amplitude response of simulation circuit vs separation between the PVDF film and the metal pin with a 100-Hz ac voltage applied to the PVDF film; (b) absolute phase response. The offset from the theoretical values, Fig. 4(b), is due to contributions from circuit detection electronics (preamp and lock-in analyzer).

dimensional effects[10] points toward using a generalized expression

$$C_{\mathrm{EFF}} = C_{\mathrm{EFF}}(R) \tag{26}$$

phenomenologically inserted in Eqs. (11) and (12). These equations can then be fitted to the experimental data for each position R, giving an empirical value of C_{EFF} at that position. The exact amplitude response can thus be calculated from the following expression:

$$A_0(R) = \frac{\omega C_{\mathrm{EFF}}(R) R_I}{(1 + \{\omega R_I [C_{\mathrm{EFF}}(R) + C_I]\}^2)^{1/2}}. \tag{27}$$

In the high-frequency limit of $\omega R_I [C_{\mathrm{EFF}}(R) + C_I] \gg 1$, which represents our experimental conditions, Eq. (27) becomes independent of ω:

$$A_0(R) \approx \frac{C_{\mathrm{EFF}}(R)}{C_{\mathrm{EFF}}(R) + C_I}. \tag{28}$$

Equation (28) allows the calculation of $C_{\mathrm{EFF}}(R)$ from experimental measurements, upon rearrangement:

$$C_{\mathrm{EFF}} = \frac{A_0(R) C_I}{1 - A_0(R)}. \tag{29}$$

B. Signal dependence on modulation frequency (f)

The experimental system employed for these measurements was the same as that in Sec. III A above. Experimental frequency-dependence data were obtained under the conditions described in Fig. 6. It can be seen from Fig. 5 that the theoretical electrical network has a flat transfer function at frequencies above 0.5 Hz. A scan in the frequency range from 0.5 to 100 Hz only depends on the response of the bandpass preamplifier ITHACO model 1201 and that of the lock-in amplifier EG&G model 5204. The latter was used in the flat mode with all frequency filters disabled. In general, one can express the total amplitude of the signal recorded by the lock-in amplifier in the form

$$U_{\mathrm{obs}}(\omega) = U_0(\omega) A_{\mathrm{system}}(\omega), \tag{30a}$$

where

$$A_{\mathrm{system}}(\omega) = A_{\mathrm{NET}}(\omega) A_{\mathrm{PA}}(\omega) A_{\mathrm{LI}}(\omega) \tag{30b}$$

and $U_0(\omega)$ was defined in Eq. (8). A_j is the transfer function of the jth instrument

$$A_j(\omega) \equiv \frac{U_{j\,\mathrm{OUT}}(\omega)}{U_{j\,\mathrm{IN}}(\omega)}; \tag{31}$$

j = system; network (NET), preamplifier (PA), lock-in analyzer (LI). Similarly, one can express the total phase lag of the signal observed by the lock-in amplifier as

$$\phi_{\mathrm{obs}}(\omega) = \phi_0(\omega) + \phi_{\mathrm{system}}(\omega), \tag{32a}$$

where

$$\phi_{\mathrm{system}}(\omega) = \phi_{\mathrm{NET}}(\omega) + \phi_{\mathrm{PA}}(\omega) + \phi_{\mathrm{LI}}(\omega). \tag{32b}$$

$\phi_0(\omega)$ is the phase lag of the signal observed between the two terminals of the capacitor C_{PVDF} at open circuit, referenced with respect to the phase of the modulated laser beam. The various phase contributions in Eq. (32b) correspond to the amplitudes discussed in conjunction with Eq. (30b). From Eqs. (30a) and (32a) we have upon rearrangement

$$U_0(\omega) = \frac{U_{\mathrm{obs}}(\omega)}{A_{\mathrm{system}}(\omega)} \tag{33}$$

and

$$\phi_0(\omega) = \phi_{\mathrm{obs}}(\omega) - \phi_{\mathrm{system}}(\omega). \tag{34}$$

Knowledge of the functions $A_{\mathrm{system}}(\omega)$ and $\phi_{\mathrm{system}}(\omega)$ for the detection system allows one to obtain the functions $U_0(\omega)$ and $\phi_0(\omega)$ via Eqs. (33) and (34). The function $A_{\mathrm{system}}(\omega) U_0(\omega)$ for our system, where $U_0(\omega) = 70$ mV (rms), is shown in Fig. 8(a). The function $\phi_{\mathrm{obs}}(\omega)$ for our system is shown in Fig. 8(b). It is clear that the simulation circuit signal amplitude is constant at frequencies above 1 Hz, with the phase decreasing rapidly toward a constant value. Figures 5 and 8 show upon comparison that the frequency dependence of the theoretical transfer function and the experimental transfer function were different from one another. These deviations from theory were found to be consistent with the domination of the transfer function by the EG&G lock-in analyzer electronics and were corrected for in subsequent P^2E measurements.

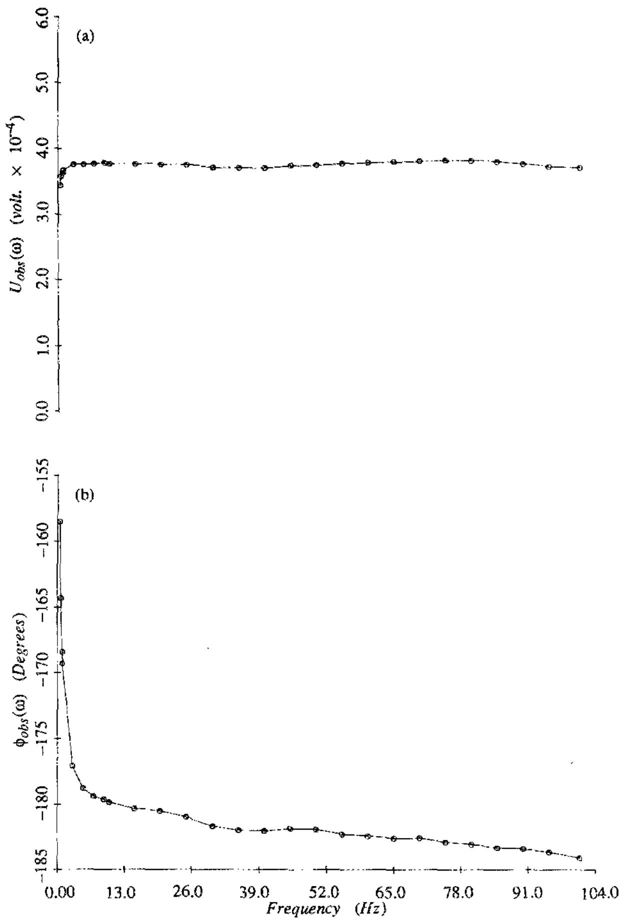

FIG. 8. (a) Experimental amplitude frequency response of the detection system with the PVDF film in contact with the metal pin; (b) phase response.

IV. P^2E CAPACITIVE DETECTION

A. PVDF film detector frequency response

The experimental setup for these measurements is shown in Fig. 2. The surface copper strip can be regarded as thermally thin[6] in the frequency range from 0.5 to 100 Hz, and it does not contribute significantly to the slope of the photothermal response of the PVDF film.[13] In that frequency range, the thermal diffusion length of copper is very large compared to that of the PVDF film and its backing (air or metal tip). The major contribution to the slope is that of the PVDF film bulk and its backing material when the PVDF film is in contact with the brass pin (a better heat sink at $R = 0$ mm compared to air), and the calculated slope of Fig. 9, curve (a), is

$$\mathrm{SLOPE}_{\mathrm{contact}} \approx -0.44\ \mathrm{s}^{1/2}. \tag{35}$$

In the case of noncontact detection ($R = 0.1$ mm) the PVDF film is backed by air and the calculated slope from Fig. 9, curve (b), is

$$\mathrm{SLOPE}_{\mathrm{noncontact}} \approx -0.55\ \mathrm{s}^{1/2}. \tag{36}$$

As can be seen from Fig. 9, the general behavior of the two curves is similar. The differences in magnitude of the slopes are attributed to different boundary conditions at the back of the PVDF film. When the metal pin is contacted to the back

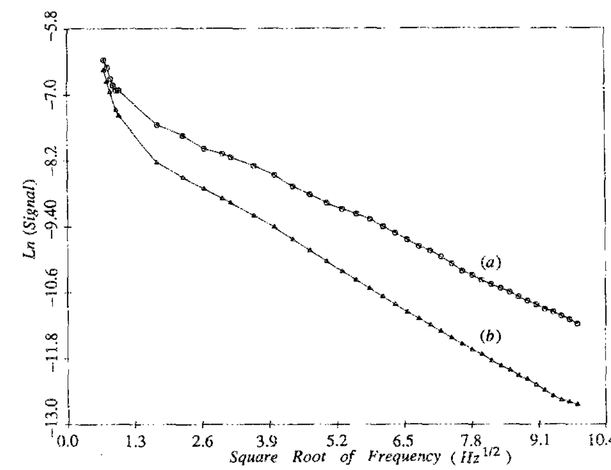

FIG. 9. Plot of the P^2E signal amplitude logarithm vs the square root of frequency (a) with the metal pin in contact with the PVDF film; and (b) with a separation $R = 0.1$ mm.

of the PVDF film, it allows heat to flow more efficiently than with air as a backing. Therefore, the P^2E signal should be enhanced and the slope of the natural logarithm of the signal versus the square root of frequency should decrease in the thermally thin limit. If the nature of the detected signal under capacitive noncontact coupling is photothermal-wave related, it is reasonable to assume that both contact and noncontact probing at the back of the PVDF detector should give the same thermal information for a sample lying on top of the copper strip above the PVDF film. The resultant response of the system is expected to be equal to the combined thermal respose of the sample and both copper and PVDF film. When an aluminum sample (1.5 mm thick) was put on top of the copper strip and excited photothermally, the resultant contact and noncontact responses were normalized by the appropriate contact and noncontact response shown in Fig. 9. The thermal response of the aluminum disk for both contact and noncontact cases after normalization collapsed into one curve, as shown in Fig. 10, as expected. However, the thermal diffusivity of the aluminum so obtained from the slope of Fig. 10 was ten times lower than the published val-

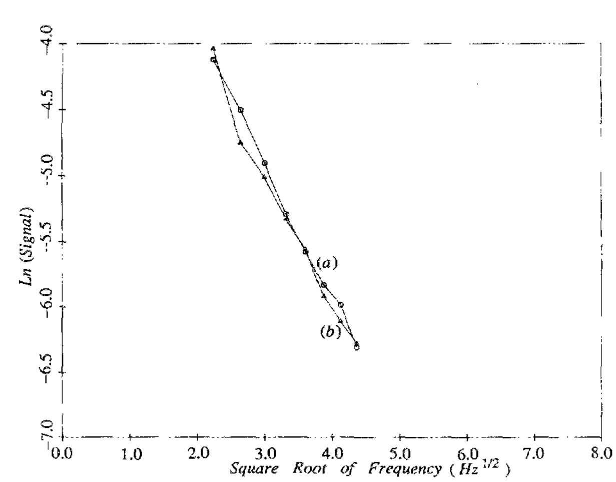

FIG. 10. P^2E signal amplitude from an aluminum sample with the metal pin in contact (a), and with separation of 0.1 mm (b). Signals were normalized with the respective signals of Fig. 9.

ue.[14] The primary reason for this discrepancy is the inherent three-dimensional nature of our system and of the P^2E signals obtained using a small diameter metal tip to sample local rather than global (i.e., integrated) values of the temperature field in the back of the specimen. The use of 1-D interpretations, such as the one employed with Fig. 10, would tend to underestimate the value for the thermal diffusivity of a sample, as no account of rapid radial thermal diffusion has been taken: This simplification amounts to an apparent greater retention of energy in the bulk of the sample than the back-detection 1-D model can account for, thus yielding a lower value for the thermal diffusivity. Furthermore, the copper strip is not perfectly flat and it could provide a rough surface contact between the aluminum sample and the copper, which would result in a large contact thermal resistance. As a consequence, the thermal diffusivity measured with this experimental setup, which was designed and optimized for thermal imaging, was lower than expected.

B. Waveform analysis of P^2E response due to optical absorption in PVDF and solid samples

In this section, we give further evidence of the photothermal nature of the capacitively coupled signals described in this work upon consideration of the waveform shapes of the recorded signals under contacting or remote conditions. The experimental setup was described in Sec. IV A above, with the intensity of the laser light modulated with a mechanical chopper. This form of light interruption corresponds to a square wave. The P^2E voltage generated across the PVDF film was observed and stored on a storage oscilloscope. dc coupling was used on both the preamplifier and the oscilloscope to avoid distortion of the signal. The thermal waveforms pertaining to direct absorption by the copper strip obtained at 100 Hz under contact and noncontact conditions are shown in Fig. 11. Both displayed waveforms look alike, since the PVDF film is thermally thick at 100 Hz. The thermal diffusion length in this case is

$$\mu_{\mathrm{PVDF}}(100\ \mathrm{Hz}) = 16\ \mu\mathrm{m} < L_{\mathrm{PVDF}} = 28\ \mu\mathrm{m}. \qquad (37)$$

Thus, the backing material does not play any significant role in the thermal wave response and the shape of the waveform. The thermal waveforms at 10 Hz under the same conditions are shown in Fig. 12. The oscilloscope traces appear different, as the PVDF sample is thermally thin:

$$\mu_{\mathrm{PVDF}}(10\ \mathrm{Hz}) = 53.3\ \mu\mathrm{m} > L_{\mathrm{PVDF}} = 28\ \mu\mathrm{m}. \qquad (38)$$

Thus, the thermal properties of the backing material make a difference in the waveform shape. The touching metal pin electrode acts as a better heat sink than air, and as a result the thermal wave propagation to the metal is facilitated due to efficient heat loss to the backing. The condition for steady-state attainment in the thermal transfer between the photothermal flux into the front, and the thermal wave flux out of the back, of the PVDF film tends to be satisfied within the optical pulse period corresponding to 10-Hz excitation, but not so at 100 Hz. As a result, the contact waveform in Fig. 12(a) appears curved as it tends to saturation at long "pulse-on" times. The 100 Hz noncontact Fig. 11(b) exhibits a

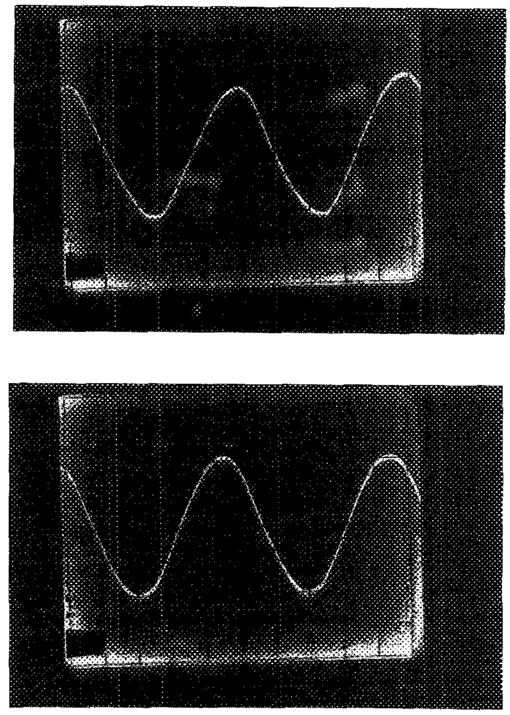

(a)

(b)

FIG. 11. Thermal waveform of the signal of Fig. 9 at 100 Hz; (a) metal pin in contact with the PVDF film; (b) with separation of 0.1 mm.

triangular appearance, as no saturation onset is in effect during the "pulse-on" period. With air as a backing at 10 Hz, a slower decay appears [triangular waveform, Fig. 12(b)]. This is due to the fact that less thermal flux to the backing air delays the onset of saturation until times beyond the 10-Hz "pulse-on" period. Qualitatively, similar waveform features have been reported by McClelland and Kniseley in the pres-

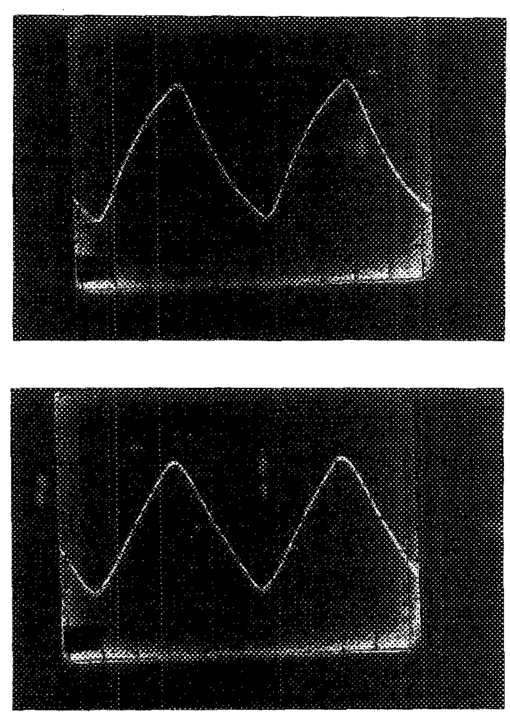

(a)

(b)

FIG. 12. Thermal waveforms similar to those of Fig. 11 at 10 Hz.

ence of backings of widely different thermal properties, using photoacoustic gas-microphone detection.[15] These observations are strong evidence of the photothermal nature of the capacitively coupled P^2E signals in this work and are consistent with the trend in slopes observed in Fig. 9.

At the present time in our system, sample and detection pin (lower electrode) are mechanically linked together through the rf shielding box (F) outlined in Fig. 2. One-dimensional scans were further accomplished by scanning the surface of a sample with focused laser light. In these experiments, the source was stationary, whereas the shielding box including sample, PVDF detector, and probe pin was scanned using a translation stage with precision $\Delta x \approx 0.02$ mm. Future noncontact, one- and two-dimensional scans of the PVDF film surface might be performed by moving the probe pin itself, a degree of freedom not available under contact conditions. This will be the subject of a future publication. Scanning results are shown in Fig. 13, which is a 100-Hz 1-D scan of the copper strip intersecting the laser beam position under contact and noncontact conditions. The broad maxima of the amplitude scans correspond to the configuration where the laser beam is located exactly above the metal probe. The broad shoulders on either side of the maximum can be tentatively attributed to long range thermal wave distribution in copper, coupled with possible copper strip contact inhomogeneities, which may account for the asymmetric signal values on either side of the center due to thermal resistance. It is interesting to note that the left-hand-side shoulder becomes more pronounced under noncontact scanning, however, the precise cause of such shoulders may be due to significant edge effect thermal wave contributions to the PVDF film[16] and/or probe tip capacitance variations as a result of enchanced electric field values at the tip periphery.[17] Figure 14 shows similar scans at 10 Hz. The broad maximum again corresponds to the position of the laser beam just above the probe pin. The shoulder feature on the left-hand side is now considerably more pronounced than in the 100-Hz scan case and it is further enhanced under noncontact probing. Comparing Figs. 13(b) and 14(b), it becomes apparent that the separation between the two peak maxima is greater at 10 Hz. This suggests that the low-frequency signal, which encompasses a larger spatial radius, is the average over a defect lying deeper in the material and positionally tilted to the left of the actual laser beam position that produced the respective leftmost maximum at 100 Hz.

For noncontact P^2E detection, the voltage reduction factor, Eq. (11), is smaller than for the contact case. This indicates that electrical signal is lost during the process. Equations (9) and (11) under contact conditions yield

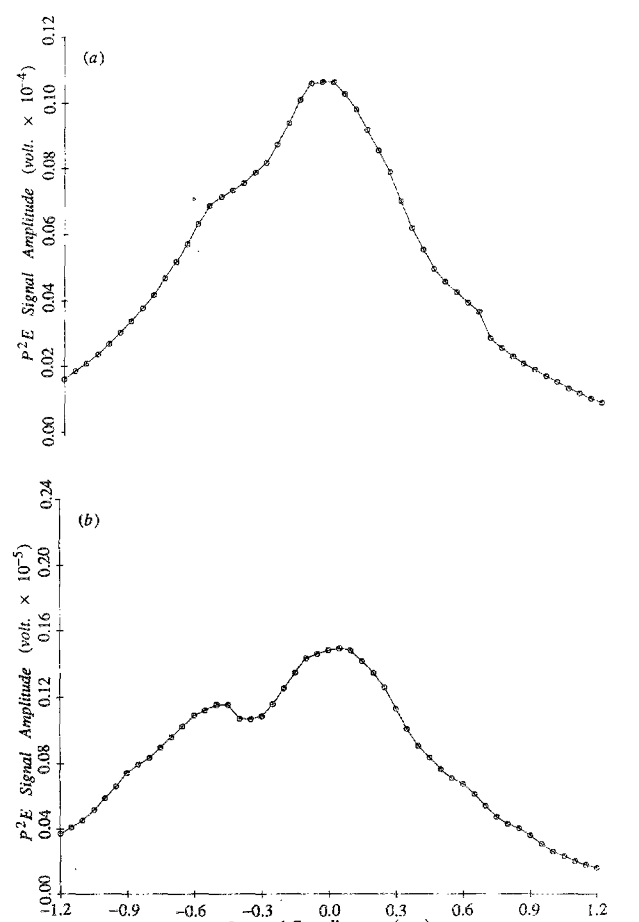

FIG. 13. (a) 1-D scan of the copper strip on the PVDF film under contact conditions; (b) similar scan under noncontact conditions. Modulation frequency: 100 Hz.

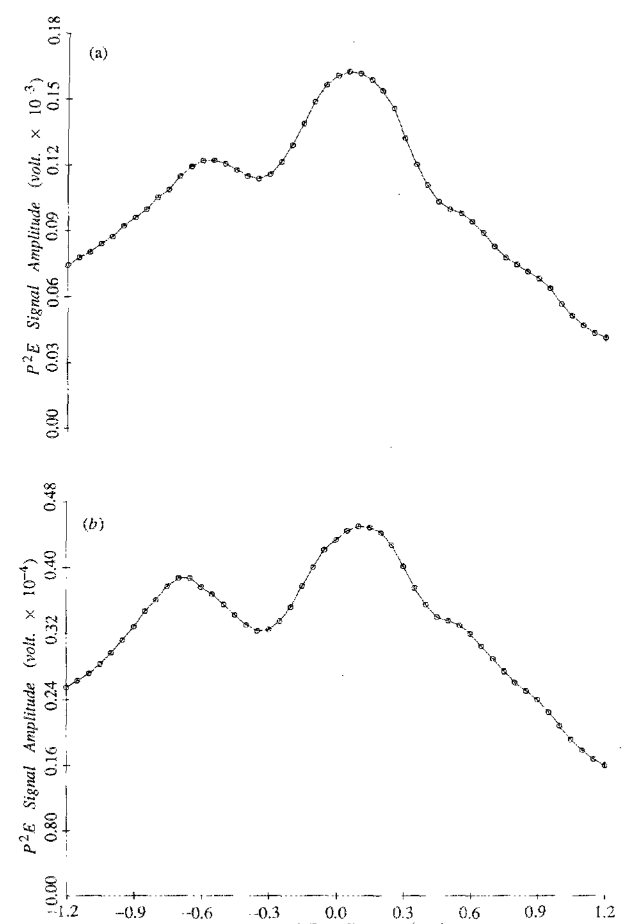

FIG. 14. (a) 1-D scan of the copper strip on the PVDF film under contact conditions; (b) similar scan under noncontact conditions. Modulation frequency: 10 Hz.

$$A_{\rm CONTACT} \approx 0.015\,59 \rightarrow 36 \text{ dB attenuation}, \tag{39}$$

where $C_{\rm EFF} \approx 1.9$ pF, $C_I \approx 120$ pF, and $R_I \approx 400$ GΩ for the frequency range between 10 and 100 Hz. For the contactless case with separation equal to 0.1 mm, Eqs. (9) and (11) yield

$$A_{\rm NONCONTACT} \approx 0.003\,58 \rightarrow 69 \text{ dB attenuation}, \tag{40}$$

where $C_{\rm EFF} \approx 0.043$ pF, $C_I \approx 120$ pF, and $R_I \approx 400$ GΩ for the frequency range between 10 and 100 Hz. As can be seen from Eqs. (39) and (40), the detection circuitry is not optimal at this time, since even under contact we have 36-dB attenuation of the signal U_0 across the PVDF film. For the contactless case, we have a further decrease of voltage signal by 33 dB. The experimental setup can be optimized by eliminating the large capacitance of the cable $C_I \approx 120$ pF. This can be accomplished by the use of a FET amplifier directly at the detection pin. One can expect that the input signal U_{in} will increase by approximately 30 dB (contact) and 40 dB (noncontact), assuming $C_I \ll 1$ pF and $R_I \gg 400$ GΩ. This indicates that the present technique can be potentially useful for high signal-to-noise ratio thermal wave imaging after further improvement.

The following characteristics and advantages of the new technique over conventional P^2E methods may be noted: The contactless nature of the new technique eliminates detector coupling imperfections which are present when two nominally flat, but microscopically rough surfaces join in intimate thermal contact and manifest themselves as local thermal resistances. Furthermore, since there is no thermal contact of the metal pin (lower electrode) with the PVDF film, one can determine the backing material's thermal effects on the system. This technique can be used for the determination of thermal properties of various backing materials especially those of liquids and gases. For scanning purposes, there is no thermal interference introduced by the probe. Another advantage is that the detector, rather than the photothermal source, can be easily scanned. In general the laser beam, the sample, and the detection pin can be moved with respect to each other. However, the spatial resolution decreases with the increase of separation between the PVDF and the detection pin. Other factors, that influence the spatial resolution, are the diameter of the laser beam, the diameter of the detection pin, the thickness of the sample, the thickness of the PVDF film, the modulation frequency of light intensity, and the system geometry. These factors will be investigated in more detail in the future.

ACKNOWLEDGMENTS

The authors wish to acknowledge the financial support of the Ontario Laser and Lightwave Research Center for this project. Partial support from the Natural Sciences and Engineering Research Council of Canada (NSERC) is also gratefully acknowledged.

APPENDIX: CIRCUIT ANALYSIS FOR METAL PIN PROBE P^2E CAPACITIVE DETECTION

Figure 15 shows a simplified equivalent circuit diagram to Fig. 2. $I_1(t)$ and $I_2(t)$ are currents present in the left and right loop of the circuit, respectively, and they are assumed to originate from the ac photopyroelectric effect, symbolized as an ac electrical power source $U(t)$. In Fig. 15, $U_{\rm in}(t)$ is the desired potential drop across the PVDF detector and the probe metal pin. The effect of the combined elements in the circuit as measured by the preamplifier is that of a capacitor C_I. The state equations describing the circuit of Fig. 15 are

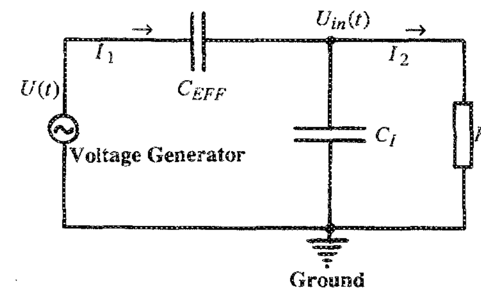

FIG. 15. Simplified equivalent circuit diagram to Fig. 2.

$$\left(\frac{1}{C_{\rm EFF}}\int_0^t I_1(y)dy + U_{\rm EFF}(0)\right) + U_{\rm in}(t) = U(t), \tag{A1}$$

$$U_{\rm in}(t) - R_I I_2(t) = 0, \tag{A2}$$

$$C_I\frac{dU_{\rm in}(t)}{dt} + I_2(t) - I_1(t) = 0. \tag{A3}$$

The term in brackets in Eq. (A1) represents the voltage drop across $C_{\rm EFF}$, and $U_{\rm EFF}(0)$ is the voltage across $C_{\rm EFF}$ at time $t=0$. Time differentiation of Eq. (A1) and substitution of the resulting equation and Eq. (A2) in Eq. (A3) yields the relation

$$(C_{\rm EFF} + C_I)\frac{dU_{\rm in}(t)}{dt} + \frac{U_{\rm in}(t)}{R_I} = C_{\rm EFF}\frac{dU(t)}{dt}. \tag{A4}$$

Assuming a harmonic dependence of the source term

$$U(t) = U_0 e^{j\omega t}, \tag{A5}$$

Eq. (A4) can be written in the compact form

$$a\frac{dU_{\rm in}(t)}{dt} + bU_{\rm in}(t) + ce^{j\omega t} = 0, \tag{A6}$$

where

$$a \equiv C_{\rm EFF} + C_I, \tag{A7a}$$

$$b \equiv 1/R_I, \tag{A7b}$$

$$c \equiv -jC_{\rm EFF}U_0\omega. \tag{A7c}$$

Laplace transformation of Eq. (A6) with the initial condition $U_{\rm in}(0) = 0$ yields

$$\hat{U}_{\rm in}(s) = \frac{c}{a(s-j\omega)(s+b/a)}. \tag{A8}$$

Equation (A8) can be written as

$$\hat{U}_{\rm in}(s) = \frac{c_1}{s-s_1} + \frac{c_2}{s-s_2}, \tag{A9}$$

where

$$c_1 \equiv -\frac{c}{a(j\omega + b/a)}, \tag{A10a}$$

$$c_2 \equiv -c_1, \tag{A10b}$$

$$s_I \equiv j\omega, \tag{A10c}$$

$$s_2 \equiv -b/a. \tag{A10d}$$

The inverse transform of Eq. (A9) is

$$U_{\text{in}}(t) = c_1 e^{j\omega t} + c_2 e^{-(b/a)t}. \tag{A11}$$

Neglecting the transient term, as is the case with the ac signal detection methods used in this work, gives the following expression for the complex steady-state voltage drop measured by the preamplifier:

$$U_{\text{in}}(t) = \left(\frac{j\omega C_{\text{EFF}} R_I}{1 + j\omega R_I (C_{\text{EFF}} + C_I)}\right) U_0 e^{j\omega t}. \tag{A12}$$

Separating out amplitude and phase components of the complex signal $U_{\text{in}}(t)$, one obtains

$$U_{\text{in}}(t) = A_0 U_0 e^{j(\omega t + \phi)}, \tag{A13}$$

where

$$A_0 = \frac{\omega C_{\text{EFF}} R_I}{\sqrt{1 + [\omega R_I (C_{\text{EFF}} + C_I)]^2}} \tag{A14}$$

and

$$\phi = \tan^{-1}\left(\frac{1}{\omega R_I (C_{\text{EFF}} + C_I)}\right). \tag{A15}$$

[1] A. Mandelis, Chem. Phys. Lett. **108**, 388 (1984).
[2] H. Coufal and A. Mandelis, in *Photoacoustic and Thermal Wave Phenomena in Semiconductors*, edited by A. Mandelis (North-Holland, New York, 1987), Chap 7.
[3] I. F. Faria, Jr., C. C. Ghizoni, and L. C. M. Miranda, Appl. Phys. Lett. **47**, 1154 (1985).
[4] S. T. Hughes and A. R. Piercy, J. Phys. D **20**, 1175 (1987).
[5] Technical Manual, Kynar Piezo Film, Pennwalt Corp., Valley Forge, PA.
[6] A. Mandelis and M. M. Zver, J. Appl. Phys. **57**, 4421 (1985).
[7] A. Mandelis, F. Care, K. K. Chan, and L. C. M. Miranda, Appl. Phys. A **38**, 117 (1985).
[8] A. C. Tam and H. Coufal, Appl. Phys. Lett. **48**, 33 (1983).
[9] K. Tanaka, Y. Ichimura, and K. Sindoh, J. Appl. Phys. **63**, 1815 (1988).
[10] A. Mandelis, Can. J. Phys. **60**, 179 (1982).
[11] A. Mandelis, J. Opt. Soc. Am. (in press).
[12] R. W. Whatmore, Rep. Prog. Phys. **49**, 1335 (1986).
[13] P. K. John, L. C. M. Miranda, and A. C. Rastogi, Phys. Rev. B **34**, 4342 (1986).
[14] A. Rosencwaig, *Photoacoustics and Photoacoustic Spectroscopy* (Wiley, New York, 1980), p. 96.
[15] J. F. McClelland and R. N. Kniseley, Appl. Opt. **15**, 2658 (1976).
[16] R. A. McFarlane and L. D. Hess, Appl. Phys. Lett. **36**, 137 (1980).
[17] J. D. Jackson, *Classical Electrodynamics*, 2nd ed. (Wiley, New York, 1975).